

Terrestrial readiness campaign for space-to-ground quantum communications with a space-qualified entangled photon-pair system

Gianluca De Santis ^{1,2} Jia Boon Chin ³ Srihari Sivasankaran ⁴ Konstantin Kravtsov ¹ Chin Chean Lim,⁴ Aitor Villar ⁴ Robert Bedington ⁴ Sana Amairi-Pyka ¹ Eleni Diamanti ² Alexander Ling ^{3,5} and James A. Grieve ¹

¹*Quantum Research Center, Technology Innovation Institute,
PO Box 9639 Abu Dhabi, United Arab Emirates*

²*Sorbonne Université, CNRS, LIP6, 4 Place Jussieu, Paris F-75005, France*

³*Center for Quantum Technologies, National University of Singapore, Singapore 117543, Singapore*

⁴*SpeQtral Pte., Ltd., Singapore*

⁵*Department of Physics, National University of Singapore, Singapore 117551, Singapore*

Realizing a global quantum internet relies on the deployment of robust satellite-based entanglement distribution links. While pioneering demonstrations have established the feasibility of such links, the transition to operational infrastructure demands the validation of robust, integrated space-to-ground architectures. Here, we report on a free-space Quantum Key Distribution experiment conducted over a 1.8 km free-space link using an engineering model of the quantum payload onboard the SpeQtre satellite and the Abu Dhabi Quantum Optical Ground Station. By implementing a BBM92 protocol with polarization-entangled photons, a secret key rate of approximately 7.56 kbps with a mean quantum bit error rate of $4.78\% \pm 0.24\%$ was produced. The deployed system featured spectral and spatial filtering approaches identical to those in the space segment, thus validating the link budget and background rejection capabilities under realistic atmospheric conditions. These results confirm the operational compatibility between the ground and space segments, establishing a critical performance baseline for the SpeQtre mission and future space-based, large-scale quantum networks.

I. INTRODUCTION

The distribution of quantum resources is fundamental to the development of future quantum networking infrastructure [1]. Various pathways have been proposed to realize a quantum internet [2–4], wherein diverse physical architectures will coexist to implement novel tasks in computation, communication, and sensing. Quantum networking constitutes the connective framework for these heterogeneous devices, with photons acting as the optimal carriers for such interactions.

Beyond simple state transfer, the distribution of entangled states enables a broader class of advanced protocols, such as blind quantum computing [5], distributed quantum computing [6], and distributed quantum sensing [7]. These capabilities extend the utility of the network far beyond secure communication, laying the groundwork for a truly interconnected quantum ecosystem. In the field of communication, a primary application of quantum resource distribution is Quantum Key Distribution (QKD), which allows for the establishment of information-theoretic secure keys between two parties [8]. While QKD represents only one of many applications enabled by quantum networking, it serves as a critical benchmark for demonstrating the maturity of quantum technologies.

Globally, several QKD networks have demonstrated the capability to distribute quantum resources. Fiber-based prepare-and-measure implementations have shown remarkable performance in terms of distance [9, 10], user capacity [11], and key-rate generation [12, 13]. Conversely, entanglement-based solutions offer enhanced se-

curity by providing a pathway toward device-independent protocols [14] and increased resilience against eavesdropping strategies [15]. Furthermore, entanglement distribution is a prerequisite for long-distance communication via quantum repeater protocols [16, 17].

However, realizing a global quantum network necessitates the distribution of resources across intercontinental distances [18]. For such scales, optical fiber is limited by fundamental attenuation [19] as well as geopolitical and infrastructural constraints [20, 21]. Consequently, satellite-based links emerge as a viable solution for achieving global connectivity [18]. Space-based QKD has undergone extensive development over the last two decades [22, 23]. Current orbital demonstrations predominantly utilize prepare-and-measure architectures [24–29], which have successfully established intercontinental links and achieved secure key generation rates on the order of kbps.

Conversely, entanglement-based (EB) protocols remain at a more nascent stage of orbital deployment and face significant implementation hurdles. Initial efforts focused on validating the feasibility of orbital entanglement distribution via Bell inequality violations [30, 31], while subsequent single-downlink and double-downlink QKD implementations yielded secure key rates in the bps range [32, 33]. In single-downlink configurations, the satellite locally measures one photon from an entangled pair while transmitting the other photon to a ground station, whereas double-downlink schemes simultaneously distribute the entangled photons to two separate ground stations. Notably, the double-downlink demonstration across a 1120 km baseline reported a

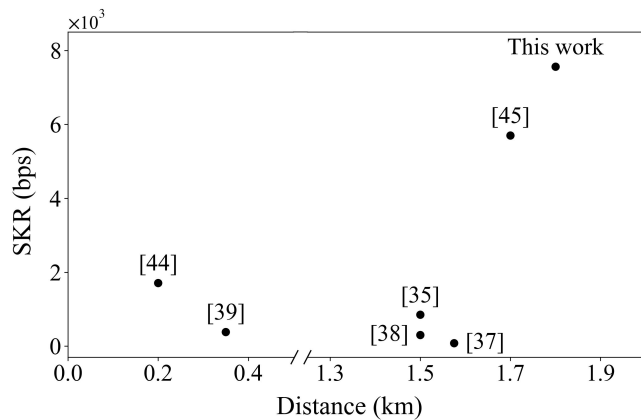


FIG. 1: Comparison of Secret Key Rate (SKR) versus distance for free-space polarization-entangled QKD systems over links up to 2 km. Data points represent reported results from the existing literature alongside the current study. The SKR values for both “This work” and Ref. [45] are calculated utilizing finite-size analysis with a 5-minute aggregation time.

QBER of $4.5\% \pm 0.4\%$ with an asymptotic key rate of 0.43 bps (0.12 bps under finite-size effects) [33].

Terrestrial horizontal links have served as essential testbeds for maturing the technology. Early experimental efforts successfully verified the viability of the distribution of polarization-entangled photons over a free-space channel under various atmospheric regimes [34–42]. More recently, research has progressed toward optimizing link performance and environmental resilience. Recent studies have demonstrated strategies for achieving high key rates using adaptive source parameters [43], quantified the impact of atmospheric aerosols on signal extinction [44], and showcased the feasibility of metropolitan-scale free-space networks using deployable, portable terminals [45]. While these studies have significantly advanced the state of the art, terrestrial demonstrations conducted to date have largely utilized specialized or ad hoc experimental configurations tailored for terrestrial flexibility and specific proof-of-concept objectives [46–48]. As the field matures toward large-scale network integration, there is a critical need to transition these bespoke setups into standardized hardware architectures. Bridging the gap between proof-of-concept demonstrations and operational satellite networks requires the rigorous characterization of quantum hardware under realistic field conditions. Specifically, validating the performance of state-of-the-art Optical Ground Stations (OGSs) and quantum payloads is crucial for establishing the reliability of entanglement-based links in space.

In this work, we demonstrate a free-space QKD experiment based on the BBM92 protocol over a 1.8 km horizontal link during nighttime operations. The transmitter node utilizes the quantum light source and receiver from an engineering model of the SpeQtre satellite quantum

payload [49], emulating a single-downlink architecture, while the receiver node employs the Abu Dhabi Quantum Optical Ground Station (ADQOGS). By implementing spatial and spectral filtering identical to that of the full-scale satellite-to-ground mission, we obtained a secret key rate (SKR) in the kbps range. The observed SKR was the highest among free-space polarization-entangled QKD demonstrations up to 2 km (Fig. 1). Furthermore, we extrapolated the results to a Low Earth Orbit (LEO) link scenario. This experimental configuration closely mimics the architecture intended for space-based quantum networking, providing critical insights for the deployment of global quantum communication networks.

II. RESULTS

Deployment A horizontal free-space QKD experiment was conducted at night under moderate atmospheric conditions on the 21st November 2025. The line-of-sight link spanned 1.8 km, with the transmitter (Alice) situated at an altitude of approximately 175 m above sea level (asl) and the receiver (Bob) positioned at approximately 50 m asl. The link was established in a semi-urban desert environment approximately 40 km from the city center of Abu Dhabi, United Arab Emirates (Fig. 2). This location provides an optimal trade-off between manageable background optical noise and logistical proximity to the city [50]. Alice and Bob were deployed as static, fixed outdoor nodes.

Space-qualified quantum light source and receiver Alice’s node, located on the Al Wathba hill, comprised a source of polarization-entangled photon pairs and a quantum receiver for polarization analysis. These are space-qualified engineering models of the SpeQtre satellite quantum payload.

The source is based on Type-0 spontaneous parametric downconversion (SPDC) and utilizes a linear displacement interferometer design [49, 51]. Photon pairs at wavelengths 780 nm (signal) and 842 nm (idler) are produced with a target state of $|\Phi^-\rangle = \frac{1}{\sqrt{2}}(|HH\rangle - |VV\rangle)$. The signal and idler photons are split via a fiber-based wavelength division multiplexer. The idler photons were locally projected into two mutually unbiased bases and detected using four single-photon silicon detectors in the quantum receiver. The signal photons were routed to a portable optical telescope with an aperture of 135 mm for beam transmission. The resulting $1/e^2$ optical spot size at the receiver plane at ADQOGS was approximately 100 mm in diameter.

ADQOGS Bob’s node was housed within the ADQOGS, a versatile, fully automated facility designed for optical and quantum communications [52]. It incorporates an 80 cm Ritchey–Chrétien telescope equipped with a Quantum Acquisition and Tracking System (QATS).

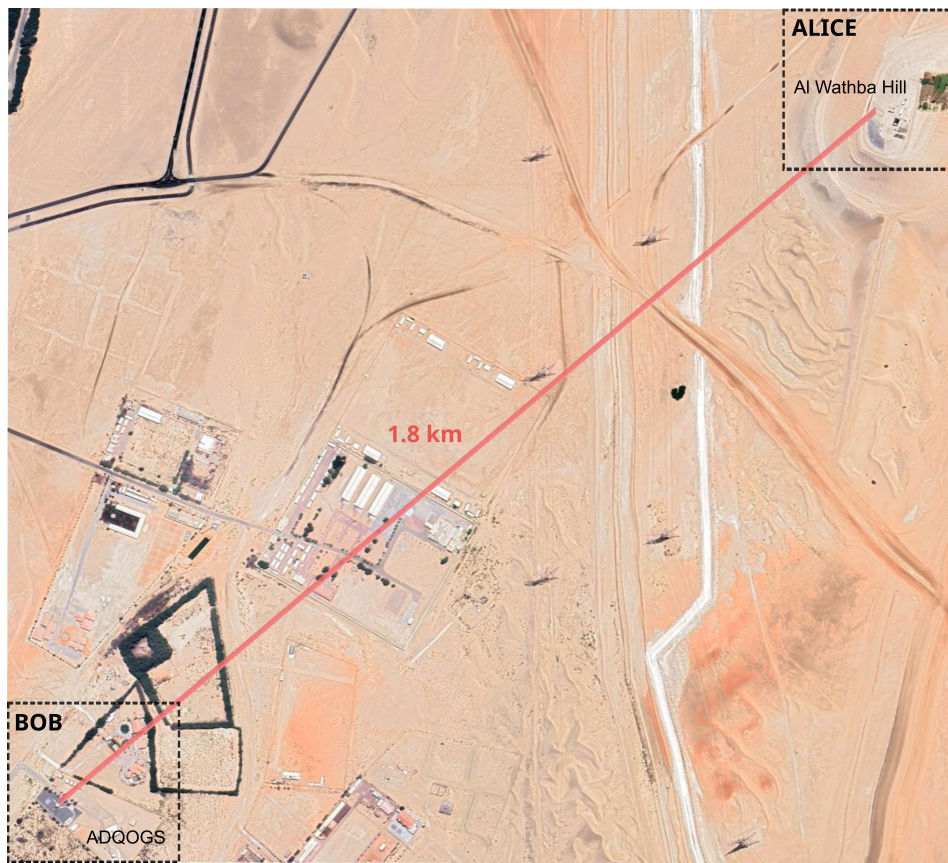


FIG. 2: Satellite image of the link between Al Wathba hill (Alice) and ADQOGS (Bob) in Abu Dhabi. Image from Google Maps.

Photons collected by the primary mirror are routed into the backend optics, where a dichroic mirror separates the quantum channel from the classical beacon. The Quantum Module (QM) features four single-photon silicon detectors (SPDs) configured to measure the polarization in two mutually unbiased polarization bases. To mitigate background noise, the module employs a 16.6 nm FWHM spectral filter centered at 785 nm. Additionally, the field of view is restricted to 0.0028° (10 arcsec in the sky) to implement spatial filtering. Under these conditions, the measured background per channel ranges from 150 to 1500 counts per second during new-moon and full-moon nights, respectively [50]. The station is also equipped with a GPS-synchronized rubidium master clock and a weather station for atmospheric monitoring.

QKD Link Using the setup described in Fig. 3, an entanglement-based BBM92 QKD protocol was implemented. Synchronization between the two nodes was achieved by calculating the cross-correlation function of the timestamps on each Time Tagger, which were disciplined using precision clock sources. Classical bi-directional communication was enabled by a pair of long-range radio bridge antennas. The initial pointing of Alice’s telescope was achieved using a 780 nm alignment

laser beam transmitted through the SPDC optical path. Following this, the alignment beam was replaced with the quantum signal from the photon-pair source, and the signal throughput was maximized by manual fine-tuning at both sides. The quantum bit error rate (QBER) was minimized by adjusting the polarization controllers inside the quantum payload. Throughout the experiment, fine-tracking was performed with a broadband visible beacon at Alice’s location to compensate for pointing drifts. For this, the QATS employed a fast steering mirror working in the closed-loop mode with a correction for spatial separation between the transmitter main aperture and the beacon. The data acquisition lasted for 20 minutes, during which the system exhibited consistent performance without significant degradation in coincidence rates or QBER (Fig. 4). A sifted coincidence rate (cps) of 24,665 photon pairs per second was observed, with a mean QBER of $4.78\% \pm 0.24\%$ over the measurement interval. The temperature and humidity were 23.6°C and 70.7% , respectively.

Key sifting was performed using symmetric basis selection at both Alice and Bob, retaining only coincidence events recorded in matching measurement bases for final key generation. All key rates were evaluated on sifted pairs, i.e., after basis reconciliation. During the bit rec-

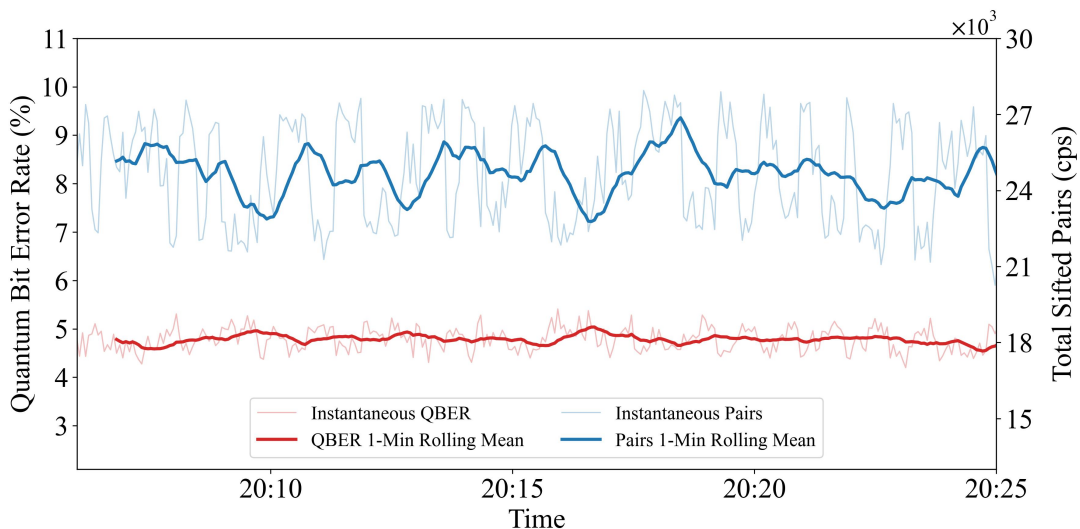


FIG. 4: Temporal evolution of system performance metrics. The left axis illustrates the quantum bit error rate, with the instantaneous 1-second resolution data plotted in light red and its corresponding 1-minute rolling mean in dark red. The right axis denotes the detected sifted pair rate in counts per second, scaled by 10^3 . The instantaneous sifted pair rate is depicted in light blue and its 1-minute rolling mean in dark blue. The system’s performance remained stable over the whole measurement session.

still required for the initial polarization alignment.

However, several ‘dynamic’ operational requirements remain to be validated to bridge the gap between this 1.8 km terrestrial link and a functional LEO-to-ground link. First, while Bob’s tracking was automated, Alice’s telescope pointing was performed manually in our test. In an operational orbital scenario, the payload must actively lock onto the ADQOGS uplink beacon to achieve the requisite fine-tracking precision. Second, although the OGS is capable of TLE-based (Two-Line Element) acquisition, this was not utilized in the current static experiment. A necessary step is the verification of autonomous orbital tracking based on TLE and dynamic Doppler shift compensation. Third, the relative motion of a satellite pass induces a continuous rotation of the polarization reference frame relative to the ground station. While we validated the internal stability of the payload’s polarization measurement bases, future iterations must implement real-time polarization tracking and correction to maintain high visibility as the satellite’s orientation changes throughout the pass. Finally, communication with satellites utilizing pulsed architectures would require an additional dynamic temporal filtering system to mitigate the time-of-flight jitter.

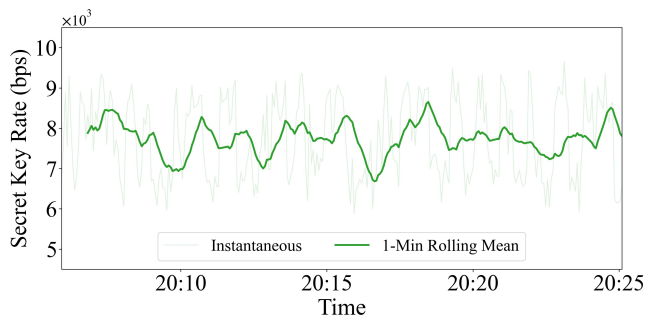
In addition to the ‘dynamic’ requirements, satellite-to-ground links face significant additional losses compared to terrestrial free-space links. The main contribution of loss results from the diffraction of the downlink beam. This is especially prominent in CubeSats such as SpeQtre, where the size constraint limits the aperture of the telescope onboard. For example, the downlink beam from SpeQtre is launched from an 8 cm-aperture telescope and has a measured M^2 value of 1.6 [56]. For a downlink dis-

tance of 500 km, the $1/e^2$ beam spot size is approximately 10 m in diameter. This would result in an additional geometric loss of 18.9 dB at ADQOGS.

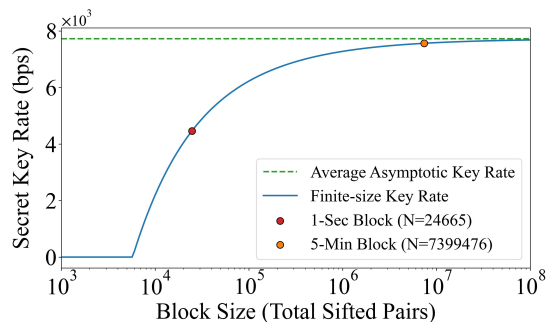
Moreover, the atmospheric profile of a 1.8 km horizontal path is significantly less demanding than a LEO downlink. The equivalence between vertical and horizontal optical paths can be estimated by equating the Aerosol Optical Depth (AOD), that is, the vertical column integral of extinction, with the Beer–Lambert attenuation along a horizontal path. Using typical clear-atmosphere values (AOD ≈ 0.1 – 0.3 and near-ground extinction coefficients ≈ 0.05 – 0.2 km^{-1}), the total atmospheric extinction for a zenith downlink is equivalent to a horizontal path on the order of 10–20 km [57]. In a LEO link, the atmospheric attenuation can contribute an additional loss of 3 dB [58].

Thus, while our 1.8 km link validated hardware logic, it operated at a reduced loss level compared to the expected LEO regime. Consequently, key generation at the high-loss regime (25–33 dB) remains a primary objective for future field tests. Moving from static terrestrial verification to the high-velocity, high-loss requirements of an orbital pass provides a benchmark for further qualifying the ground segment readiness for the SpeQtre mission and future satellite QKD operations.

To model the expected key rates in these high-loss regimes, we extrapolate our results to a LEO link. SpeQtre’s passes over ADQOGS were simulated from the satellite’s TLE, with maximum elevation angles ranging from 32° to 80° . Considering the link to be established only when the elevation angle was at least 20° , these passes lasted between 225 s to 299 s. With the varying geometric losses and assuming 6 dB of loss from tracking er-



(a) Asymptotic Secret Key Rate.



(b) Finite-size Secret Key Rate.

FIG. 5: Secret key rate performance of the free-space quantum link. (a) The asymptotic secret key rate calculated over the duration of the experimental run. The instantaneous rate (light green) exhibits fluctuations driven by atmospheric channel turbulence, while the 1-minute rolling mean (dark green) highlights the overall system stability. (b) Finite-size secret key rate evaluated as a function of the aggregated block size N , using the sharp finite-key bound (see Supplementary Materials). The solid blue curve shows the theoretical finite-key prediction, illustrating the impact of statistical finite-size effects for small datasets. The red marker corresponds to 1-second acquisition blocks ($N \approx 2.4 \times 10^4$), while the orange marker represents 5-minute aggregation ($N \approx 7.4 \times 10^6$). Increasing the block size reduces statistical fluctuations, enabling the finite-size key rate to approach the asymptotic limit (dashed green line).

rors and atmospheric attenuation [58], the total number of sifted coincidences obtained for the pass varied from 4552 counts to 11754 counts. Following the same finite-key analysis, the maximum SKR achieved was 4.3 bps (for the pass with a maximum elevation of 80°). These extrapolated results highlight an additional challenge of satellite QKD: the SKR and the total length of secret key obtained can differ greatly from pass to pass.

Looking beyond the immediate requirements for orbital deployment, several advanced technological frontiers can be pursued to enhance the performance and utility of the OGS infrastructure. A primary objective is the integration of adaptive optics (AO) systems at the receiver. By actively mitigating turbulence-induced wavefront distortions, AO offers a pathway to stabilize and optimize coupling efficiency into single-mode fibers [59, 60], a critical requirement for interfacing free-space links with fiber-based quantum repeaters and terrestrial metropolitan networks. Furthermore, extending the operational window of the station to daylight hours remains a pivotal goal for maximizing the mission duty cycle. This transition will require the implementation of ultra-narrow spectral filtering and the optimization of temporal coincidence windows to maintain high signal-to-noise

ratios against solar background radiance. Finally, future iterations could explore the scalability of this architecture for multi-node quantum networks, where the OGS acts as a flexible relay for entanglement swapping or multi-satellite handover protocols [61]. These advancements will transition the current architecture from a point-to-point demonstrator into a robust, high-bandwidth node for a global quantum internet.

We also note that the analysis presented in this work follows the standard assumptions adopted for BBM92 implementations [62]. A dedicated investigation of detector squashing models [63] and the effect of detector-side imperfections [64] on the secret key rate is left for future work.

In summary, we have successfully demonstrated the operational integration of a space-qualified quantum payload with an automated optical ground station. The achieved key rates and stability metrics verify the hardware compatibility and background rejection strategies required for space-to-ground quantum communication. These results confirm the readiness of the architecture for the SpeQtre mission, marking a decisive step toward the deployment of reliable satellite-based quantum networks.

[1] S.-H. Wei, B. Jing, X.-Y. Zhang, J.-Y. Liao, C.-Z. Yuan, B.-Y. Fan, C. Lyu, D.-L. Zhou, Y. Wang, G.-W. Deng, *et al.*, *Laser & Photonics Reviews* **16**, 2100219 (2022).
 [2] H. J. Kimble, *Nature* **453**, 1023 (2008).
 [3] C. Simon, *Nature Photonics* **11**, 678 (2017).
 [4] S. Wehner, D. Elkouss, and R. Hanson, *Science* **362**, eaam9288 (2018).

[5] A. Broadbent, J. Fitzsimons, and E. Kashefi, in *2009 50th annual IEEE symposium on foundations of computer science (IEEE, 2009)* pp. 517–526.
 [6] A. Yimsiriwattana and S. J. Lomonaco Jr, in *Quantum information and computation II*, Vol. 5436 (SPIE, 2004) pp. 360–372.
 [7] Z. Zhang and Q. Zhuang, *Quantum Science and Technol-*

- ogy **6**, 043001 (2021).
- [8] N. Gisin, G. Ribordy, W. Tittel, and H. Zbinden, Reviews of modern physics **74**, 145 (2002).
- [9] H.-L. Yin, T.-Y. Chen, Z.-W. Yu, H. Liu, L.-X. You, Y.-H. Zhou, S.-J. Chen, Y. Mao, M.-Q. Huang, W.-J. Zhang, *et al.*, Physical review letters **117**, 190501 (2016).
- [10] Y. Liu, W.-J. Zhang, C. Jiang, J.-P. Chen, C. Zhang, W.-X. Pan, D. Ma, H. Dong, J.-M. Xiong, C.-J. Zhang, *et al.*, Physical Review Letters **130**, 210801 (2023).
- [11] B. Fröhlich, J. F. Dynes, M. Lucamarini, A. W. Sharpe, S. W.-B. Tam, Z. Yuan, and A. J. Shields, Scientific reports **5**, 18121 (2015).
- [12] Z. Yuan, A. Plews, R. Takahashi, K. Doi, W. Tam, A. Sharpe, A. Dixon, E. Lavelle, J. Dynes, A. Murakami, *et al.*, Journal of Lightwave Technology **36**, 3427 (2018).
- [13] W. Li, L. Zhang, H. Tan, Y. Lu, S.-K. Liao, J. Huang, H. Li, Z. Wang, H.-K. Mao, B. Yan, *et al.*, Nature photonics **17**, 416 (2023).
- [14] V. Zapatero, T. van Leent, R. Arnon-Friedman, W.-Z. Liu, Q. Zhang, H. Weinfurter, and M. Curty, npj quantum information **9**, 10 (2023).
- [15] A. Acin, N. Gisin, and L. Masanes, Physical review letters **97**, 120405 (2006).
- [16] J.-W. Pan, D. Bouwmeester, H. Weinfurter, and A. Zeilinger, Physical review letters **80**, 3891 (1998).
- [17] K. Azuma, S. E. Economou, D. Elkouss, P. Hilaire, L. Jiang, H.-K. Lo, and I. Tzitrin, Reviews of Modern Physics **95**, 045006 (2023).
- [18] L. de Forges de Parny, O. Alibart, J. Debaud, S. Gresnani, A. Lagarrigue, A. Martin, A. Metrat, M. Schiavon, T. Troisi, E. Diamanti, *et al.*, Communications Physics **6**, 12 (2023).
- [19] S. Pirandola, R. Laurenza, C. Ottaviani, and L. Banchi, Nature communications **8**, 15043 (2017).
- [20] OECD, *Public Rights of Way for Fibre Deployment to the Home*, Tech. Rep. (OECD, 2008) accessed 2026-01-13.
- [21] African Union, “Cross border and interconnection policies,” PDF, accessed 2026-01-13.
- [22] R. Bedington, J. M. Arrazola, and A. Ling, npj Quantum Information **3**, 30 (2017).
- [23] J. S. Sidhu, S. K. Joshi, M. Gündoğan, T. Brougham, D. Lowndes, L. Mazzarella, M. Krutzik, S. Mohapatra, D. Dequal, G. Vallone, *et al.*, IET Quantum Communication **2**, 182 (2021).
- [24] S.-K. Liao, W.-Q. Cai, W.-Y. Liu, L. Zhang, Y. Li, J.-G. Ren, J. Yin, Q. Shen, Y. Cao, Z.-P. Li, *et al.*, Nature **549**, 43 (2017).
- [25] S.-K. Liao, J. Lin, J.-G. Ren, W.-Y. Liu, J. Qiang, J. Yin, Y. Li, Q. Shen, L. Zhang, X.-F. Liang, *et al.*, Chinese Physics Letters **34**, 090302 (2017).
- [26] S.-K. Liao, W.-Q. Cai, J. Handsteiner, B. Liu, J. Yin, L. Zhang, D. Rauch, M. Fink, J.-G. Ren, W.-Y. Liu, *et al.*, Physical review letters **120**, 030501 (2018).
- [27] Y. Li, S.-K. Liao, Y. Cao, J.-G. Ren, W.-Y. Liu, J. Yin, Q. Shen, J. Qiang, L. Zhang, H.-L. Yong, *et al.*, Optica **9**, 933 (2022).
- [28] A. Khmelev, A. Duplinsky, R. Bakhshaliev, E. Ivchenko, L. Pismeniuk, V. Mayboroda, I. Nesterov, A. Chernov, A. Trushechkin, E. Kiktenko, *et al.*, Optics Express **32**, 11964 (2024).
- [29] Y. Li, W.-Q. Cai, J.-G. Ren, C.-Z. Wang, M. Yang, L. Zhang, H.-Y. Wu, L. Chang, J.-C. Wu, B. Jin, *et al.*, Nature , 1 (2025).
- [30] J. Yin, Y. Cao, Y.-H. Li, S.-K. Liao, L. Zhang, J.-G. Ren, W.-Q. Cai, W.-Y. Liu, B. Li, H. Dai, *et al.*, Science **356**, 1140 (2017).
- [31] A. Villar, A. Lohrmann, X. Bai, T. Vergoossen, R. Bedington, C. Perumangatt, H. Y. Lim, T. Islam, A. Reezwana, Z. Tang, *et al.*, Optica **7**, 734 (2020).
- [32] J. Yin, Y. Cao, Y.-H. Li, J.-G. Ren, S.-K. Liao, L. Zhang, W.-Q. Cai, W.-Y. Liu, B. Li, H. Dai, *et al.*, Physical review letters **119**, 200501 (2017).
- [33] J. Yin, Y.-H. Li, S.-K. Liao, M. Yang, Y. Cao, L. Zhang, J.-G. Ren, W.-Q. Cai, W.-Y. Liu, S.-L. Li, *et al.*, Nature **582**, 501 (2020).
- [34] C.-Z. Peng, T. Yang, X.-H. Bao, J. Zhang, X.-M. Jin, F.-Y. Feng, B. Yang, J. Yang, J. Yin, Q. Zhang, *et al.*, Physical review letters **94**, 150501 (2005).
- [35] I. Marcikic, A. Lamas-Linares, and C. Kurtsiefer, Applied Physics Letters **89** (2006).
- [36] R. Ursin, F. Tiefenbacher, T. Schmitt-Manderbach, H. Weier, T. Scheidl, M. Lindenthal, B. Blauensteiner, T. Jennewein, J. Perdigues, P. Trojek, *et al.*, Nature physics **3**, 481 (2007).
- [37] C. Erven, C. Couteau, R. Laflamme, and G. Weihs, Optics express **16**, 16840 (2008).
- [38] A. Ling, M. P. Peloso, I. Marcikic, V. Scarani, A. Lamas-Linares, and C. Kurtsiefer, Physical Review A—Atomic, Molecular, and Optical Physics **78**, 020301 (2008).
- [39] M. P. Peloso, I. Gerhardt, C. Ho, A. Lamas-Linares, and C. Kurtsiefer, New Journal of Physics **11**, 045007 (2009).
- [40] T. Scheidl, R. Ursin, A. Fedrizzi, S. Ramelow, X.-S. Ma, T. Herbst, R. Prevedel, L. Ratschbacher, J. Kofler, T. Jennewein, *et al.*, New Journal of Physics **11**, 085002 (2009).
- [41] C. Erven, B. Heim, E. Meyer-Scott, J. Bourgoin, R. Laflamme, G. Weihs, and T. Jennewein, New Journal of Physics **14**, 123018 (2012).
- [42] Y. Cao, H. Liang, J. Yin, H.-L. Yong, F. Zhou, Y.-P. Wu, J.-G. Ren, Y.-H. Li, G.-S. Pan, T. Yang, *et al.*, Optics express **21**, 27260 (2013).
- [43] S. Ecker, B. Liu, J. Handsteiner, M. Fink, D. Rauch, F. Steinlechner, T. Scheidl, A. Zeilinger, and R. Ursin, npj Quantum Information **7**, 5 (2021).
- [44] S. Mishra, A. Biswas, S. Patil, P. Chandravanshi, V. Mongia, T. Sharma, A. Rani, S. Prabhakar, S. Ramachandran, and R. P. Singh, Journal of Optics **24**, 074002 (2022).
- [45] A. Kržič, S. Sharma, C. Spiess, U. Chandrashekhara, S. Töpfer, G. Sauer, L. J. González-Martín del Campo, T. Kopf, S. Petschornig, T. Grafenauer, *et al.*, npj Quantum Information **9**, 95 (2023).
- [46] G. G. Rozenman, A. Maslennikov, S. P. Gandelman, Y. Reches, S. Delfan, N. K. Kundu, L. Zhang, and R. Liu, “Free-space and satellite-based quantum communication: Principles, implementations, and challenges,” (2026).
- [47] P. V. Trinh, A. T. Pham, A. Carrasco-Casado, and M. Toyoshima, in *2018 Progress in Electromagnetics Research Symposium (PIERS-Toyama)* (IEEE, 2018) pp. 1672–1679.
- [48] M. Mehic, M. Niemiec, S. Rass, J. Ma, M. Peev, A. Aguado, V. Martin, S. Schauer, A. Poppe, C. Pacher, and M. Voznak, ACM Computing Surveys **53**, 1 (2020).
- [49] A. Villar, in *Quantum Computing, Communication, and Simulation VI* (SPIE, 2026) p. PC1391907.
- [50] G. De Santis, K. Kravtsov, O. Kara, S. Amairi Pyka, and J. A. Grieve, in *IAF Space Communications and Naviga-*

- tion Symposium* (International Astronautical Federation (IAF), 2025) pp. 318–326.
- [51] A. Lohrmann, C. Perumangatt, A. Villar, and A. Ling, *Appl. Phys. Lett.* **116**, 021101 (2020).
- [52] S. Amairi-Pyka, C. Fischer, K. Kravtsov, G. De Santis, A. Grosso, E. Fischer, K. Kudielka, and J. A. Grieve, in *International Conference on Space Optics — ICSO 2024*, Vol. 13699, International Society for Optics and Photonics (SPIE, 2025) p. 136993N.
- [53] X. Ma, C.-H. F. Fung, and H.-K. Lo, *Physical Review A—Atomic, Molecular, and Optical Physics* **76**, 012307 (2007).
- [54] V. Mannalath, V. Zapatero, and M. Curty, *Physical Review Letters* **135**, 020803 (2025).
- [55] T. Islam, J. S. Sidhu, B. L. Higgins, T. Brougham, T. Vergoossen, D. K. Oi, T. Jennewein, and A. Ling, *PRX Quantum* **5**, 030101 (2024).
- [56] A. Fitzpatrick, R. Harwin, H. Robarts, W. Brzozowski, S. Todd, S. Vallapureddy, L. Saraff, O. Chang, W. Li, D. Pearson, M. Salter, and A. Vick, in *International Conference on Space Optics — ICSO 2024*, edited by F. Bernard, N. Karafolas, P. Kubik, and K. Minoglou (SPIE, 2025) p. 241.
- [57] A. Czerwinski, *Optical and Quantum Electronics* **57**, 577 (2025).
- [58] C.-Y. Lu, Y. Cao, C.-Z. Peng, and J.-W. Pan, *Reviews of Modern Physics* **94**, 035001 (2022).
- [59] V. Marulanda Acosta, D. Dequal, M. Schiavon, A. Montmerle-Bonnefois, C. B. Lim, J.-M. Conan, and E. Diamanti, *New Journal of Physics* **26**, 023039 (2024).
- [60] V. M. Acosta, D. Dequal, M. Schiavon, A. Montmerle-Bonnefois, C. B. Lim, J.-M. Conan, and E. Diamanti, *arXiv preprint arXiv:2411.09564* (2024).
- [61] G. De Santis, K. Kravtsov, S. Amairi-Pyka, and J. A. Grieve, *EPJ Quantum Technology* **12**, 50 (2025).
- [62] C. C.-W. Lim, F. Xu, J.-W. Pan, and A. Ekert, *Physical Review Letters* **126**, 100501 (2021).
- [63] T. Tsurumaru and K. Tamaki, *Physical Review A* **78**, 032302 (2008).
- [64] F. Xu, X. Ma, Q. Zhang, H.-K. Lo, and J.-W. Pan, *Reviews of Modern Physics* **92**, 025002 (2020).

Supplementary Material

I. KEY-RATE ANALYSIS

We summarize the procedure used to estimate the secret key rate for the BBM92 protocol. Two cases are considered: the asymptotic limit and the finite-key analysis using the sharp statistical bound.

A. Preliminaries

For each data block, we denote:

- N : total number of sifted pairs,
- n : number of bits used for parameter estimation,
- $n_{\text{key}} = N - n$: number of key-generation bits,
- \hat{p} : observed quantum bit error rate (QBER),
- ϵ : total security parameter.

We used $n = 0.20N$ (20% for parameter estimation, 80% for key generation). The binary entropy function is defined as:

$$h(x) = -x \log_2 x - (1-x) \log_2 (1-x), \quad (1)$$

The security parameter is divided as:

$$\epsilon = \epsilon_{\text{PE}} + \epsilon_{\text{sec}} + \epsilon_{\text{cor}}, \quad (2)$$

corresponding to parameter estimation, secrecy, and correctness, respectively. We used an equal splitting $\epsilon_{\text{PE}} = \epsilon_{\text{sec}} = \epsilon_{\text{cor}} = \epsilon/3$, with a total security parameter of $\epsilon = 4 \times 10^{-16}$.

B. Asymptotic Key Rate

In the asymptotic limit, the secret key length is given by [1]:

$$S_{\text{asym}} = \max \{0, n_{\text{key}} [1 - f_{\text{EC}} h(\hat{p}) - h(\hat{p})]\}, \quad (3)$$

where f_{EC} denotes the error correction efficiency. Note that the basis reconciliation factor is equal to one because the rate is calculated using sifted pairs, i.e., after basis reconciliation.

C. Finite-Key Rate with Sharp Bound

We next consider the tighter statistical bound introduced in [2].

By defining:

$$\kappa_{n,\epsilon} = \frac{2}{9n} \ln \left(\frac{1}{\epsilon_{\text{PE}}} \right), \quad (4)$$

the function $\gamma_{n,\epsilon}^+(x)$ is given by:

$$\gamma_{n,\epsilon}^+(x) = \frac{1}{1 + 4\kappa_{n,\epsilon}} \left[3\kappa_{n,\epsilon} + (1 - 2\kappa_{n,\epsilon})x + 3\sqrt{\kappa_{n,\epsilon}(\kappa_{n,\epsilon} + x - x^2)} \right]. \quad (5)$$

Note that the bound $\gamma_{n,\epsilon}^+(x)$ is valid for $\kappa_{n,\epsilon} \leq 1/4$; if this condition is violated due to an exceedingly small sample size n , we set $q_{\text{Sharp}}^{\text{th}} = 1$.

The confidence interval is defined piecewise as:

$$\Gamma_{n,\epsilon}^+(x) = \begin{cases} \gamma_{n,\epsilon}^+(x) & \text{if } x \in \left[0, \frac{1-2\kappa_{n,\epsilon}}{1+\kappa_{n,\epsilon}}\right] \\ 1 + \epsilon & \text{otherwise.} \end{cases} \quad (6)$$

Following Proposition 2 of [2], the phase error threshold for the remaining bits is:

$$q_{\text{Sharp}}^{\text{th}} = \frac{N \Gamma_{n,\epsilon}^+(\hat{p}) - n \hat{p}}{N - n}. \quad (7)$$

The phase error threshold in Eq. 7 is bounded to the interval $[0, 1]$. The corresponding finite-key secret key length is:

$$S_{\text{Sharp}} = \max \{0, n_{\text{key}} [1 - h(q_{\text{Sharp}}^{\text{th}})] - f_{\text{EC}} n_{\text{key}} h(\hat{p}) - \Delta\}. \quad (8)$$

II. LEO SATELLITE EXTRAPOLATION

In the 1.8 km QKD experiment, a mean sifted coincidence rate of 24665 cps was obtained. We extrapolate this to a LEO link by considering the expected geometric loss in a downlink from SpeQtre to ADQOGS.

Using the Two-Line Element (TLE) of SpeQtre on 9 April 2026, 18:27, SpeQtre's pass over ADQOGS was calculated over the next seven days. Five of these passes, with varying maximum elevation angles ranging from 32° to 80° (Fig. 1), were analyzed to determine the expected number of sifted coincidence events over each pass.

For each pass, the geometric loss was calculated. An additional 6 dB of loss was added on top of the geometric loss to account for atmospheric attenuation and tracking errors. The number of sifted coincidences collected was integrated over the pass. Finite-key analysis was done to extract the key rate for each pass. The results are tabulated in Table I.

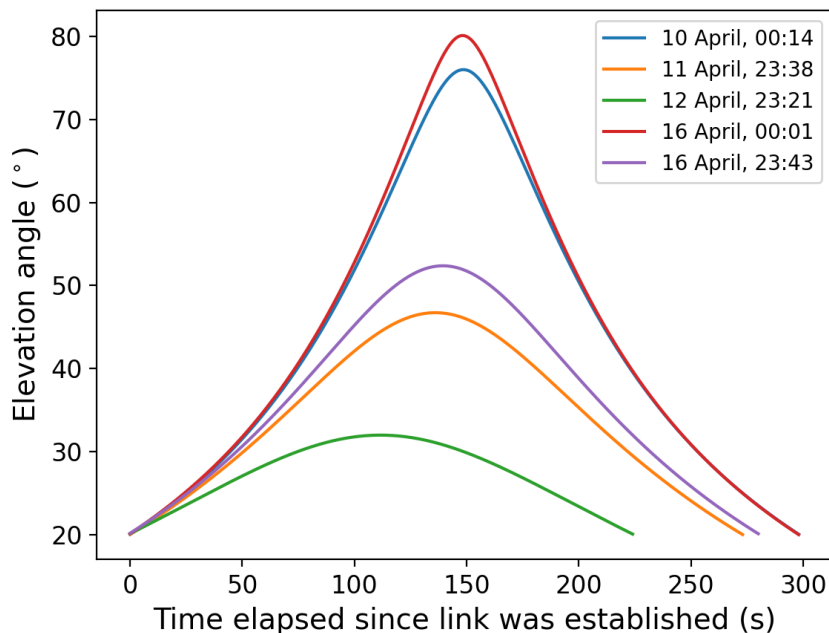


FIG. 1: Elevation angles throughout some simulated passes of SpeQtre over ADQOGS, simulated using SpeQtre's TLE from 9 April 2026, 18:27. The labels refer to the local time (UTC+4) when the link is first established. The link remains established when the elevation angle $\geq 20^\circ$.

Local time of satellite pass	Maximum elevation angle	Link duration	Secret key rate (bps)
10 April, 00:14	76°	299 s	4.14
11 April, 23:38	47°	274 s	1.45
12 April, 23:21	32°	225 s	0
16 April, 00:01	80°	299 s	4.31
16 April, 23:43	52°	281 s	2.17

TABLE I: Secret key rates expected for various passes of SpeQtre over ADQOGS.

-
- [1] X. Ma, C.-H. F. Fung, and H.-K. Lo, *Physical Review A—Atomic, Molecular, and Optical Physics* **76**, 012307 (2007).
[2] V. Mannalath, V. Zapatero, and M. Curty, *Physical Review Letters* **135**, 020803 (2025).